



Enhancing the deN₂O activity of the supported Co₃O₄|α-Al₂O₃ catalyst by glycerol-assisted shape engineering of the active phase at the nanoscale



Sylwia Gudyka ^a, Gabriela Grzybek ^a, Joanna Grybos ^a, Paulina Indyka ^a, Bartosz Leszczyński ^b, Andrzej Kotarba ^a, Zbigniew Sojka ^{a,*}

^a Faculty of Chemistry, Jagiellonian University, Ingardena 3, 30-060 Krakow, Poland

^b Faculty of Physics, Astronomy and Applied Computer Science, Jagiellonian University, Lojasiewicza 11, 30-348 Krakow, Poland

ARTICLE INFO

Article history:

Received 9 May 2016

Received in revised form 10 August 2016

Accepted 16 August 2016

Available online 17 August 2016

Keywords:

Cobalt spinel

Alumina

N₂O decomposition

Dispersion

Faceting

ABSTRACT

A series of supported Co₃O₄|α-Al₂O₃ catalyst synthesized by glycerol-assisted method was thoroughly characterized (X-ray micro-tomography, XRD, RS, FTIR, SEM/TEM/EDX, TG/DTA, TPR), and their reactivity was evaluated in N₂O decomposition in 5% N₂O/He and 1.5% N₂O, 1% NO_x, 1 vol.% H₂O, 2.0 vol.% O₂. Their superior catalytic activity in comparison to the benchmark Co₃O₄|α-Al₂O₃ catalyst, obtained via incipient wetness impregnation with the aqueous solution, was accounted for by differences in cobalt spinel dispersion on the alumina support, spinel nanoparticle size and faceting. Whereas for the samples prepared from the aqueous solution the spinel active phase exhibits a broad bimodal size distribution (with the maxima for 10–50 nm crystallites and 300–600 nm agglomerates) in the case of glycerol-assisted synthesis a monomodal distribution is featured by isolated spinel nanocrystallites of 10–30 nm. At the same time, the presence of glycerol changes the spinel crystallites morphology from rhombicuboctahedron with abundant exposition of the less favorable (111) planes into the truncated cubic shape with the dominant more active (100) facets. It was shown that the beneficial effect of glycerol is sustained in typical gaseous residuals (H₂O, NO_x, O₂) present in the tail gases of nitric acid plants. The observed effect of glycerol-assisted synthesis was accounted for by complexation of cobalt by glycerol, leading to the formation of an intrapore cobalt glycerolate, which upon calcination is transformed into well dispersed Co₃O₄ cubic nanocrystals.

© 2016 Elsevier B.V. All rights reserved.

1. Introduction

Nitrous oxide, along with carbon dioxide and methane, belongs to the principal greenhouse gases [1]. N₂O is emitted from natural nitrogen processes, as well as mobile and stationary anthropogenic sources – mainly nitric and adipic acid plants. The most challenging way of removing nitrous oxide from nitric acid installations is the end-pipe technology based on a catalytic low-temperature decomposition in the flow of tail gases [2]. Cobalt spinel was found to be one of the most active catalysts for this process [3–5]. It has been shown that its catalytic activity can significantly be enhanced by structural (Zn, Ni) [6,7] and surface (K, Cs) promotion [8–11]. However, the large-scale applications of the bulk cobalt spinel catalyst

are limited by a relatively high price of cobalt. An immediate, simple solution for this problem is dispersion of cobalt spinel active phase over a support surface. Spreading of cobalt spinel on high surface area supports such as alumina [12,13], silica [14], magnesia [15] or ceria [16–18] has been reported so far. Reduction of the physical dimensions of the spinel phase to a nanometer scale leads to an increase in the surface to volume ratio, and hence the number of the accessible active sites. Apart from choosing a proper carrier, it is also important to select a suitable precursor and the deposition method. From large gamut of currently available preparation techniques, precipitation and impregnation are the most commonly used in the catalytic industry. In line with a practical context, the preparation procedure should involve simple chemicals and a minimal number of unit operations that are carried out in typical conditions. However, at the same time, it should assure a homogeneous dispersion of the active phase with a uniform particle size of desired morphology, controlled preferably in the nanoscale range. These parameters can be engineered by the proper selection of the pre-

* Corresponding author at: Faculty of Chemistry, Jagiellonian University, ul. Ingardena 3, 30-060 Krakow, Poland.

E-mail address: sojka@chemia.uj.edu.pl (Z. Sojka).

cursors and physicochemical conditions of the deposition process [19].

Transition metal alkoxides have recently been proposed to provide a novel precursor-mediated synthetic route for fabrication of nanostructured oxide materials [20]. Many of *d*-block elements, such as Ti, V, Mn, Fe, Ni, Cu, Zn can easily coordinate to the hydroxyl groups of various mono- and poly-hydroxyl alcohols, forming stable complexes and/or extended coordination networks. The resultant solid state alkoxides can be then easily transferred to the corresponding nano-oxides by simple thermal treatment. The size and morphology of the latter may be tuned by the adjustment of the type of the alcohol complexant, hydrolysis conditions, as well as temperature and time of the subsequent calcination.

This paper focuses on application of the cobalt alkoxides as a precursor for preparation of the cost-effective supported $\text{Co}_3\text{O}_4/\alpha\text{-Al}_2\text{O}_3$ catalyst for low-temperature N_2O decomposition. Due to its abundance at the market as a side-product in biodiesel synthesis, glycerol was selected as a promising, cheap component of the cobalt nitrate solution for an alumina support impregnation that can be easily used also at industrial scale. The effect of glycerol-assisted deposition on cobalt spinel particle size, faceting, and dispersion on the α -alumina support, in comparison to benchmark impregnation from aqueous solution, was investigated, and its impact on the catalytic activity in deN_2O was revealed.

2. Experimental part

2.1. Catalysts preparation

The alpha alumina support, prepared from commercial powder pseudoboehmite (Sasol Versal) by calcination in air at 1400 °C for 4 h, was provided by Institute of New Chemical Synthesis (INS Pulawy, Poland). The support was impregnated by incipient wetness method using water-glycerol solutions of $\text{Co}(\text{NO}_3)_2$ with different content of the glycerol: 15, 30, 50 and 100 vol.% (glycerol-assisted method). Additionally, a benchmark catalyst was prepared by classic impregnation with a $\text{Co}(\text{NO}_3)_2 \cdot 6\text{H}_2\text{O}$ aqueous solution without glycerol addition (glycerol-free method). The cobalt(II) nitrate concentration was adjusted to obtain 15 wt.% loading of the Co_3O_4 active phase for all catalysts. After impregnation the samples were dried at 120 °C for 12 h and then calcined in air at 600 °C for 4 h. Thermogravimetric screening combined with QMS analysis of the evolving gases revealed that no coke is formed upon the calcination of the catalysts.

2.2. Catalysts characterization

The cobalt spinel loading was determined using an Energy-Dispersive XRF spectrometer (Thermo Scientific, ARL QUANT'X). The X-rays were generated with a Rh anode (4–50 kV with 1 kV step), 1 mm size beam and a 3.5 mm Si(Li) drifted crystal detector with a Peltier cooling ~185 K were used. For quantitative analysis, a UniQuant software along with a series of the calibration metallic standards were employed.

X-ray powder diffraction measurements were carried out by means of a Bruker D8-advance instrument with the $\text{CuK}\alpha$ radiation ($\lambda = 1.540598 \text{ \AA}$) in the 2 theta range between 10° and 90° with the step of 0.05°.

Raman spectra at the wavelength excitation of 785 nm (100–1000 cm^{-1} , 1 cm^{-1} resolution) were recorded at room temperature using a Renishaw InVia spectrometer and a confocal Leica DMLM microscope equipped with a CCD detector. The signal to noise ratio was optimized by accumulating nine scans for each measurement.

Thermogravimetric analysis was carried out on a Mettler Toledo TGA/DSC1 instrument. The experiments were conducted under oxidizing conditions (40 ml/min air and 20 ml/min Ar) in the temperature range between 25 and 1025 °C with the step of 10°/min. The temperature was measured directly below the crucible with the sample, and compared with a reference crucible containing the equivalent amount of the alumina carrier only.

Temperature programmed reduction experiments (TPR) were carried out in a quartz reactor using the catalyst samples of ~150 mg. Before the measurements the samples were heated in flow of He up to 500 °C in order to remove adsorbed water and carbon dioxide. The TPR profiles were recorded using a QMS detector (Hiden Analytical), while heating the samples in the flow of 5% H_2/Ar (50 ml/min) in the temperature range from 25 to 700 °C.

Morphology of the supported catalysts was examined by Scanning and Transmission Electron Microscopies. The SEM observations were carried out by TESCAN Vega 3 LMU (20 keV) electron microscope after coating with gold. A high-resolution TEI Tecnai OESIS analytical transmission microscope, equipped with an X-FEG Schottky field emitter (accelerating voltage of 200 keV) and a Super-X EDX (Energy Dispersive X-ray) system with the windowless 4-sector silicon drift detector (SDD), were used for sample imaging at the nanoscale. The Z-contrast images were acquired by means of a high angle annular dark field (HAADF) detector in the scanning transmission electron microscopy (STEM) mode. To maximize the HAADF signal intensity, a spot size of ~1.5 nm and the camera length kept in a range of 220 mm–550 mm were used. The STEM images coupled with the EDX elemental mapping were acquired with a sample drift correction using the Bruker Esprit software. Prior to microscopic analysis, the samples were ultrasonically dispersed in ethanol and dropped on a holey carbon film supported on a copper grid (Agar Scientific, 300 mesh).

Quantitative assessment of the grain size distribution was determined by processing the X-ray Co-K α dot maps correlated with the STEM images of the cobalt spinel particles, using the DigitalMicrograph software (Gatan) with the implemented local neighborhood density threshold and dilation script [21]. The equivalent particle diameters were determined by automatic tracing of the maximum radius of a circular spinel nanoparticles and/or clusters. The image gradient analysis and edge detection of the spinel nanocrystals were performed by using Canny algorithm [22] implemented in the FeatureJ [23] software of the image processing program ImageJ [24].

The alumina extrudes were also analyzed by X-ray microtomography techniques. The measurements were performed using a SkyScan 1172–Kontich instrument (80 keV, pixel size 1.5 μm , 360°, 10 averaged frames, rotation step 0.3°). Based on the obtained data the porosity and the pore size distribution were calculated using the CT-Analyzer software (SkyScan), and visualized in the form of 3D pictures by volume rendering method available in the CTVox software.

2.3. N_2O decomposition tests

The catalytic activity tests of N_2O decomposition were carried out in a temperature programmed surface reaction (TPSR) mode (10°/min) in a quartz flow reactor. The reaction was performed using 300 mg of the catalysts (sieve fraction of 0.2 – 0.3 mm) in the atmospheric pressure for a model feed (5% N_2O in He, flow 30 ml/min, $\text{GHSV} = 7'000 \text{ h}^{-1}$), and a gas mixture with typical contaminants of the nitric acid plant tail gases (1.5% N_2O , 1% NO_x , 1 vol.% H_2O , 2.0 vol.% O_2 , flow 90 ml/min, $\text{GHSV} = 20'000 \text{ h}^{-1}$). The reaction products were monitored by a quadrupole mass spectrometer (RGA200, SRS, lines with $m/z = 44$ (N_2O), 32 (O_2), 30(NO), 28 (N_2), 18(H_2O)). To ensure that the reactor is operating in the kinetic

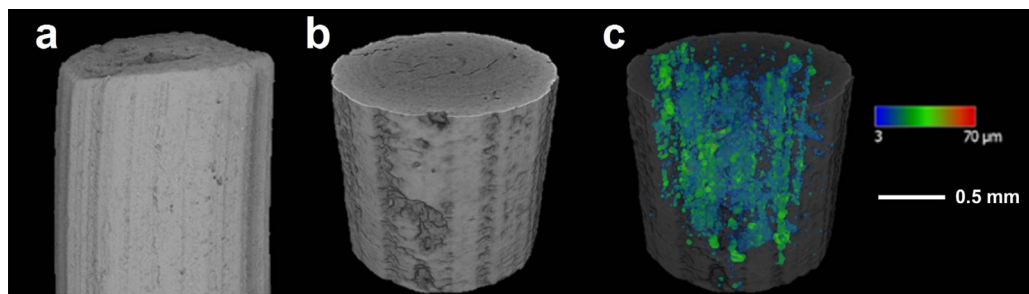


Fig. 1. (a) SEM image of α -Al₂O₃ molder. (b, c) μ CT 3D visualization of: model of support and pore net inside support, respectively.

regime, the criterial numbers for extra- and intragranular diffusion limitations were checked according to the Eurokin procedure [25].

3. Results and discussion

The shape of an alumina extrude used as a support for the cobalt spinel active phase dispersion is shown in Fig. 1a (SEM) and 1b (X-ray microtomography). It can be epitomized by a cylinder with the diameter of 1.5 mm and the length of 25 mm (1a). The internal macroporosity of the extrude (Fig. 1c) consists of a network of pores in the range of 3–50 μ m. They are preferentially aligned along the main axis of the extrude. The total volume of macropores available for aqueous solution filling was equal to 0.42 cm³/g.

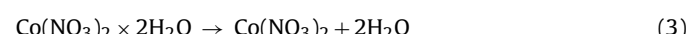
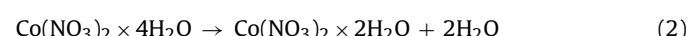
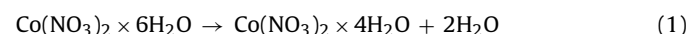
These extrudes were used for dispersion of the cobalt spinel precursor via the incipient wetness method. Two types of the Co(NO₃)₂·6H₂O impregnation solutions without and with glycerol addition (with the C₃H₈(OH)₃ content of 15, 30, 50% and 100 vol.%) were used. Upon drying the samples were calcined in air to transform the deposited cobalt complexes into the corresponding spinel. The elemental content of cobalt spinel in the resultant supported catalysts was determined by XRF techniques. The results are presented in Table 1. In all samples the amount of the cobalt spinel phase was close to the nominal value of 15 wt.%, showing the reliability of the synthesis protocol. The BET surface area for all the catalyst was in the range of 3.5–4 m²/g and was close to that of the bare alumina support (3.1 m²/g). The porosity determined by mercury intrusion method was equal to 0.26 and 0.24 cm³/g for the catalyst obtained via glycerol-free and glycerol-assisted synthesis, respectively.

The crystalline structure of the prepared supported catalysts was investigated by XRD and micro-Raman techniques. The X-ray diffraction patterns for the supported catalysts synthesized with glycerol-assisted (30%, 100%) and glycerol-free (0%) methods are presented in Fig. 2a. The diffraction lines at $2\theta = 35.1, 37.7, 43.4, 52.5, 57.5, 59.4, 61.2, 66.5, 68.2$ correspond to the (104), (110), (113), (024), (116), (211), (122), (214) and (300) reflection planes, respectively, indexed within the trigonal structure space group ($R-3c$) of α -Al₂O₃ (ICSD – 9771). Formation of the cobalt spinel upon decomposition of the precursor was revealed by the presence of the characteristic lower intensity lines (marked by * in Fig. 2a) located at $2\theta = 31.3, 36.9, 44.9, 55.6, 59.5, 65.4, 74.4$ and 77.3, correspond-

ing to the (220), (311), (400), (422), (511), (440), (533) and (622) reflection planes of Co₃O₄ (ICSD – 69378). Raman spectra of the samples synthesized with different amount of glycerol (0–100%) are collated in Fig. 2b. The lines located at 195, 487, 526, 624 and 694 cm⁻¹ correspond to the five vibrational modes F_{2g}, E_g, F_{2g}, F_{2g} and A_{1g}, respectively [26], which are diagnostic for cobalt spinel, confirming definitely its presence.

The conversion profiles of catalytic N₂O decomposition screening are presented in Fig. 3 as a function of temperature. All the catalysts prepared via the glycerol-assisted method exhibit much higher activity in comparison to the benchmark catalyst prepared by classic incipient wetness with an aqueous solution (Fig. 3a). The best catalytic performance was observed for the sample prepared via 100% glycerol-assisted method. For this catalyst at a temperature range of practical interest, 350–450 °C, the N₂O conversion is four times higher than for sample prepared via the glycerol-free method. In the case of the samples prepared with 30–50% glycerol impregnation mixture, the positive effect persists but the activity improvement is less spectacular (~2-fold increase in activity). The reactivity tests were next performed in the conditions simulating tail gases of nitric acid plants (presence of typical residual contaminants such as NO_x, O₂, H₂O, and a higher value of GHSV = 20 000 h⁻¹). In such more severe conditions, the discrepancies in the performance between the catalysts obtained by two methods are even more pronounced (Fig. 3b). Whereas for the glycerol-free sample $T_{50\%}$ increases up to 600 °C, for the glycerol-assisted catalysts it is shifted down to 450 °C. Additionally, in the first case, there is a strong temperature shift in the reaction onset. The N₂O decomposition starts at 400 °C, whereas for the glycerol-assisted samples it already reaches the 20% conversion. Taking into account that the XRF, XRD and μRS results showed in all the investigated catalyst the presence of the cobalt spinel only, with practically the same loading, the observed dramatic changes in the reactivity may result from a different number of accessible active sites (catalyst dispersion) and their different chemical local environment (faceting). This point was next addressed by means of TG/DTA, TPR, IR and STEM-EDX measurements.

The thermogravimetric curves of spinel formation during calcination of the alumina support impregnated with aqueous and glycerol solutions of the cobalt nitrate show completely different shapes (Fig. 4a and b). For aqueous solution the three main endothermic peaks appearing in the temperature range 80–150 °C can be assigned to progressive dehydration of the intrapore cobalt nitrate, which following the literature [27], can be schematized in the following way:



These three dehydration steps (the first is well-separated, the second and third are partially overlapped) correspond to the total

Table 1
Co₃O₄ loading in series of prepared Co₃O₄/ α -Al₂O₃ catalysts determined by XRF method.

Content of glycerol in aqueous solution of Co(NO ₃) ₂	wt.% of Co ₃ O ₄
0%	14.8
15%	14.4
30%	15.7
50%	14.3
100%	15.4

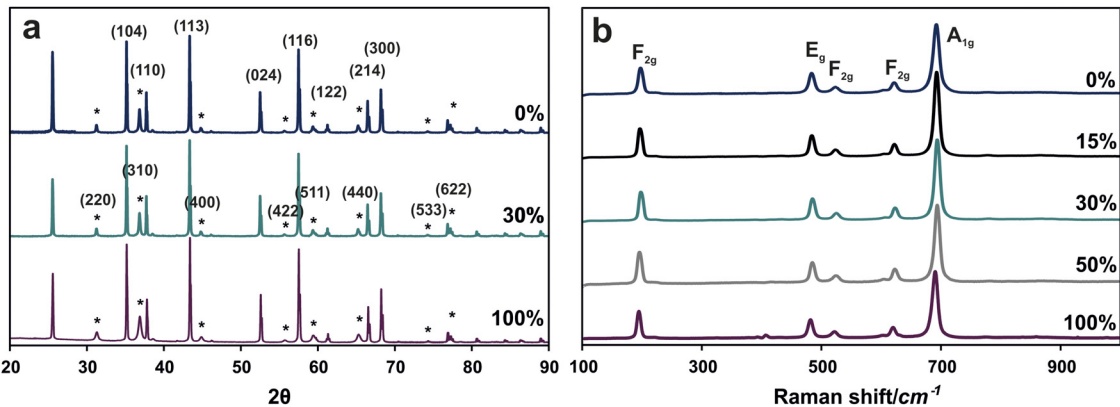


Fig. 2. (a) Diffraction patterns of $\text{Co}_3\text{O}_4/\alpha\text{-Al}_2\text{O}_3$ catalysts prepared with amount of glycerol in range 0–100% (b) Raman spectra of $\text{Co}_3\text{O}_4/\alpha\text{-Al}_2\text{O}_3$ catalysts prepared with amount of glycerol in range 0–100%.

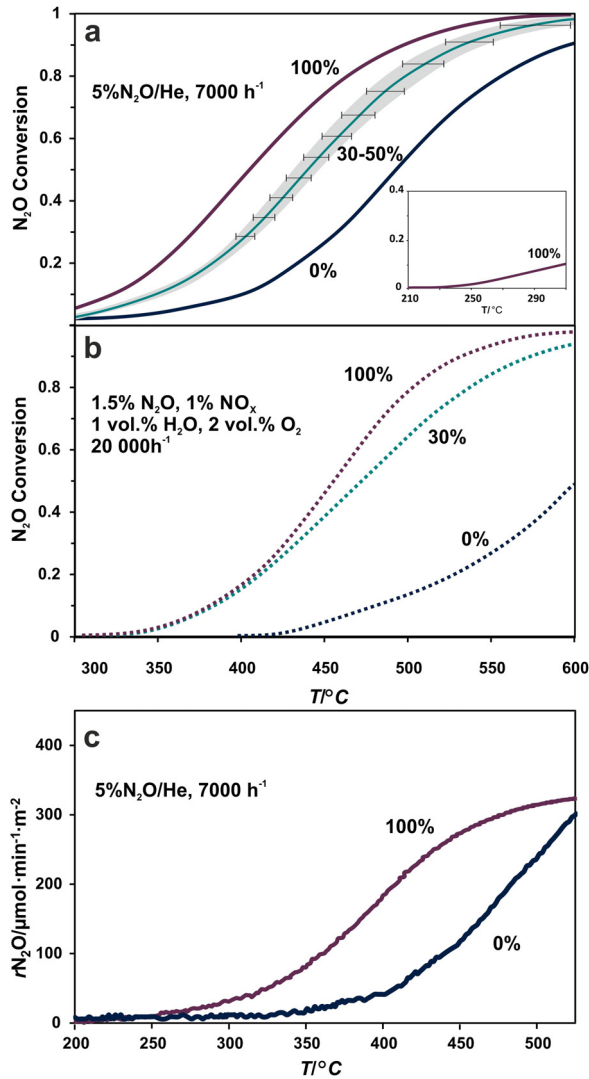


Fig. 3. Comparison of catalytic activity of $\text{Co}_3\text{O}_4/\alpha\text{-Al}_2\text{O}_3$ catalysts, prepared with amount of glycerol in range 0–100%, depicted as N_2O conversion curves in temperature function. Catalytic test performed in model gas (5% $\text{N}_2\text{O}/\text{He}$) (a and c) and with contaminants (1.5% N_2O , 1% NO_x , 1 vol.% H_2O , 2.0 vol.% O_2) (b).

mass loss of 36%, in-line with the change in the sample stoichiometry (implied by Eq. (1)–(3)) upon heating. The next more pronounced peak at 200 °C, accompanied by the largest mass loss

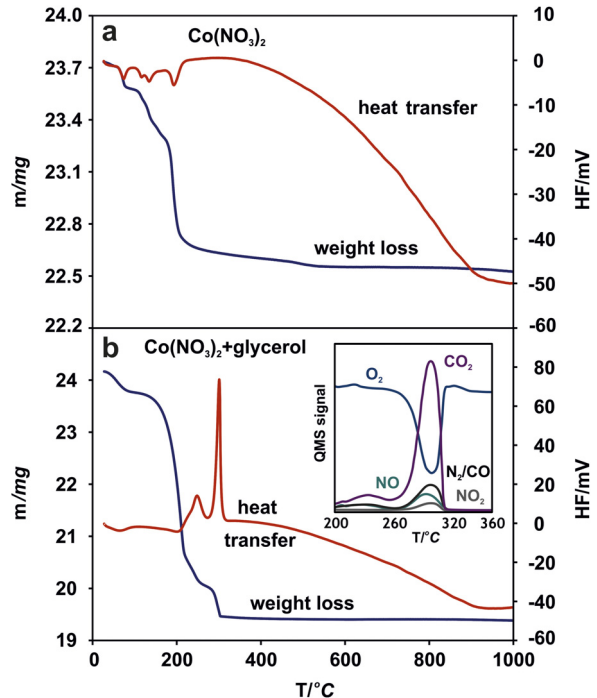
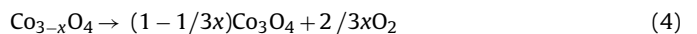


Fig. 4. TG/DTA analysis of the $\alpha\text{-Al}_2\text{O}_3$ support impregnated with aqueous (a) and glycerol (b) solutions of cobalt nitrate used as a precursor of cobalt spinel active phase and QMS analysis of the evolving gases (insert).

(56%), corresponds to the thermal decomposition of the dried cobalt nitrate into defected cobalt spinel with the evolution of the gas phase NO/NO_2 species [28]. In the oxidizing conditions calcination at low temperatures leads to the formation of cobalt deficient $\text{Co}_{3-x}\text{O}_4$ spinel, discussed previously by us elsewhere [29]. Thus, the observed small changes in the sample mass in the range of 200–600 °C can be accounted for by transformation of the defected $\text{Co}_{3-x}\text{O}_4$ into a stoichiometric Co_3O_4 , accompanied by the release of excess oxygen:



In the case of glycerol-assisted synthesis the low-temperature endothermic peaks, characteristic for cobalt nitrate dehydration are essentially absent, and the DTA profile is dominated by the strong exothermic maxima in the range 220–310 °C (Fig. 4b). The observed peaks in this temperature range can be assigned to the thermal oxidation of a cobalt-glycerolate complex, as shown in [30]. This is confirmed by the rapid evolution of CO_2 and N_2/NO_x , accompa-

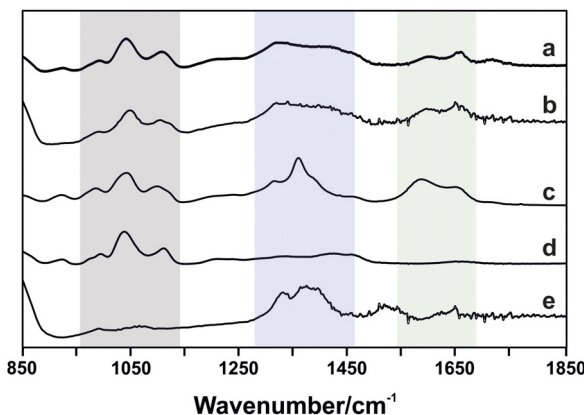


Fig. 5. IR spectra of α -Al₂O₃ support impregnated with glycerol (a) and aqueous-glycerol solution of cobalt nitrate (b) along with the reference spectra of cobalt-glycerolate (c), alumina impregnated with glycerol (d), and alumina impregnated with aqueous solution of cobalt nitrate (e).

nied by the consumption of oxygen, revealed by the QMS analysis of the evolving gases (Fig. 4b insert). Since the observed total mass loss of 49% corresponds to stoichiometric Co:glycerol ratio close to one, it can be concluded that the intrapore cobalt monoglycerolate was formed upon impregnation of the alumina support with the glycerol-cobalt nitrate solution. Once formation of the cobalt spinel phase was accomplished no CO₂ release was observed upon further increase of the temperature, confirming that the catalyst is not contaminated by a residual carbon.

The IR spectra of the investigated cobalt precursors and the reference glicerolate are presented in Fig. 5. They exhibit characteristic signals of the alcoholic C—O stretching mode at 1037 and 1112 cm⁻¹ (Fig. 5a-d), which are distinctly shifted in comparison to the bulk glycerol (1028 and 1107 cm⁻¹ [31]). Such blue shift can be accounted for by replacement of the hydrogen atom in the —OH group by cobalt in the glycerolate, inducing an electron flow towards the C—O bond, making it thereby stronger. The IR spectra of the Co(NO₃)₂/glycerol| α -Al₂O₃ (Fig. 5a) and Co(NO₃)₂/(glycerol + H₂O)| α -Al₂O₃ catalysts (Fig. 5b) show similar features, absent in the spectra of the Co(NO₃)₂ + H₂O| α -Al₂O₃ one (Fig. 5e). The peaks at 1310 and 1581 cm⁻¹ absent in the IR spectra of glycerol on alumina, and alumina impregnated with an aqueous solution of cobalt nitrate, confirm the formation of

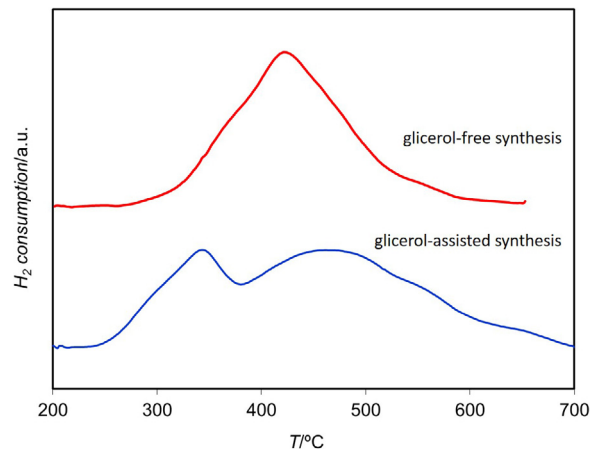


Fig. 6. TPR profiles of alumina supported cobalt spinel catalyst obtained by glycerol-free and glycerol-assisted synthesis methods.

cobalt glycerolate. This conclusion is also supported by the changes in the charge transfer band at 304 nm in UV-vis spectra (not shown). In the 1100 cm⁻¹ region of the IR spectra of glycerol| α -Al₂O₃ (Fig. 5d) the shift associated with the glycerol complexation ($R(-OH)_3 + Al^{3+} \rightarrow (R-O)_3Al + 3H^+$) indicates that C₃H₈O₃ may act as an adhesion promoter, facilitating penetration and binding of the cobalt spinel precursor to the alumina support.

Two different mechanisms of spinel formation in the absence and presence of glycerol may lead to different nanoscale morphologies of the resultant spinel active phase, as well as its various dispersion over the alumina support. Indirectly, this is reflected in distinct TPR profiles observed for both types of the catalysts (Fig. 6). Whereas for glycerol-assisted catalyst the reduction profile exhibits two distinct peaks at ~350 and ~470 °C assigned to transformation of $Co^{3+} \rightarrow Co^{2+}$ and $Co^{2+} \rightarrow Co^0$, respectively [32], in the case of the catalyst synthesized in the absence of glycerol these two peaks are barely resolved as they moved toward each other. This implies that the both reduction processes are overlapped suggesting not only different dispersion but also the different shapes of cobalt spinel nanocrystals.

The more informative STEM pictures revealed, apart from spinel nanocrystallites, the presence of compacted sub-micrometric agglomerates (Fig. 7a₁₋₂). Clearly, the extent of agglomeration

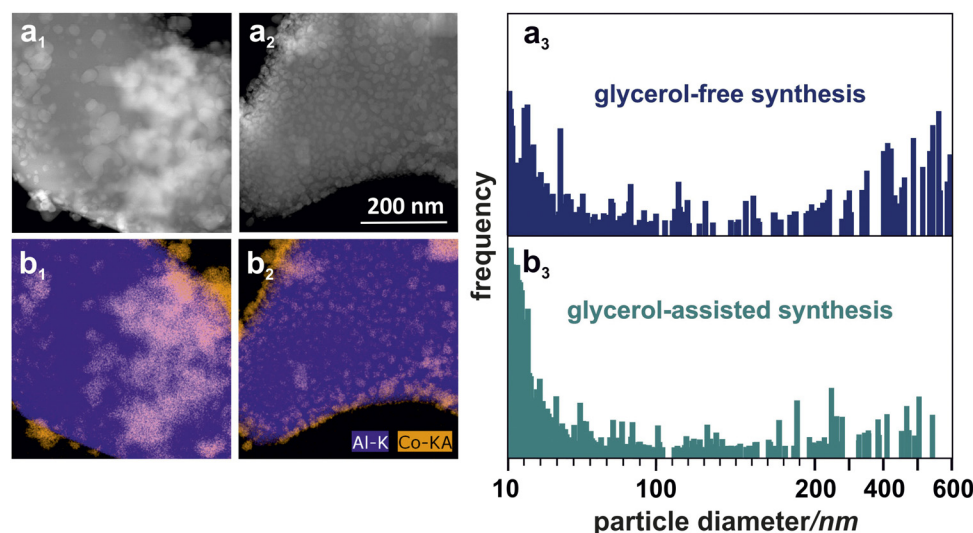


Fig. 7. STEM images of alumina supported cobalt spinel catalyst obtained by impregnation with aqueous solution (a) and glycerol solution (b) of cobalt nitrate along with the corresponding Co₃O₄ nanoparticle distribution histograms.

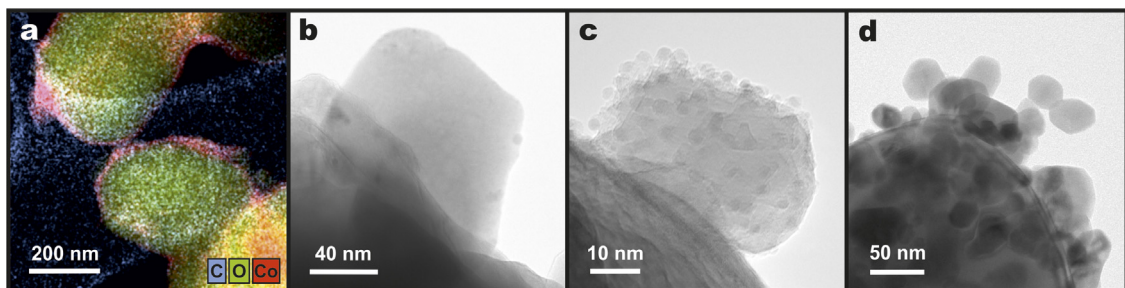


Fig. 8. (a) STEM – EDX map of the cobalt glycerolate precursor (pink) coating the alumina support (yellow-green). (b) TEM image of the amorphous precursor attached to the alumina support (c) Magnified TEM image of the precursor with the embedded small (up to few nanometres) Co_3O_4 nanocrystals (see also XRD data in Fig. S1), (d) TEM image of the Co_3O_4 nanocrystals deposited on the alumina support after the complete decomposition of the cobalt glycerolate precursor into the spinel phase.

strongly depends on the applied method of the catalyst synthesis. In the case of the sample prepared with glycerol the nanocrystallites are better dispersed, and the agglomerates are smaller and much less abundant (Fig. 7b_{1–2}). Quantification of the obtained results in the form of the particle size histograms for both types of catalysts is shown in Fig. 7a₃ and b₃. The histograms were constructed by sorting automatically the determined particle diameters into the classes of equal size differing by 5 nm, taking into account around 3000 individual particles. For each class (bin), the number of particles that fall into each bin was counted and weighted by the particle/cluster area assigned to the particular class range. In the case of the incipient wetness impregnation with an aqueous solution (glycerol-free method) the size distribution is very broad with two maxima for small separated nanocrystals (10–50 nm) and large compacted agglomerates (300–600 nm). On the contrary, for glycerol-assisted synthesis, the nanocrystallites are more homogeneously spread over the alumina grains (Fig. 7b_{1–2}). The nanoparticles of 10–30 nm dominate the profile, whereas the contribution of larger agglomerates is distinctly attenuated and their dimensions are rather uniformly spread.

The gross features of thermal transformation of the cobalt glycerolate precursor into the spinel nanoparticles were next monitored by electron microscopy and XRD techniques. In Fig. 8 the microscopic images of the samples calcinated at 200 °C (a–b) are presented, whereas the images (c) and (d) correspond to thermal treatment at ~350 °C and ~500 °C, respectively. The EDX-STEM analysis of the sample calcinated at 200 °C (Fig. 8a) revealed that the $\alpha\text{-Al}_2\text{O}_3$ grains are coated with the Co-glycerol precursor that forms a nanometric layer of varying thickness. A magnified view of the layer of the amorphous precursor is also shown in Fig. 8b. The changes in the cobalt precursor morphology induced by heating at ~350 °C consist in nucleation and growth of the cobalt spinel nanocrystallites (diameter < 5 nm) dispersed in the amorphous matrix (Fig. 8c and also Fig. S1). The XRD measurements confirmed the simultaneous presence of the amorphous and crystalline spinel phases (Fig. S2). Upon further increase of the temperature to 500 °C, an increase of the Co_3O_4 grains to ~20 nm was observed, while the amorphous matrix is completely decomposed. In the course of thermal transformation of the Co-glycerolate precursor, a large number of nuclei for spinel crystallization are formed at the early stage. During the growth of the incipient nanocrystals they are separated by the amorphous matrix, which apparently disfavors their coalescence. As a result, the spinel nanocrystals are better dispersed and become more uniform in size. This may be accounted for, i.a., by the fact that a simultaneous presence of the glycerol and the cobalt nitrate in an intimate contact leads to the local combustion synthesis. This is revealed by the appearance of strong exothermic peaks around 300 °C accompanied by an instant generation of CO_2 , N_2 , NO_x and water (see Fig. 4b and the insert). The rapidly evolving gases, acting as an propellant, may enhance the

separation of the emerging spinel nanocrystals [33,34]. The same spreading effect was also observed when large amounts of cobalt glycerolate was decomposed in a crucible.

More detailed imaging of the shape of the alumina dispersed Co_3O_4 nanocrystals by means of HAADF/STEM is shown in Figs. 9 and 10. The left column corresponds to the original HAADF STEM pictures (a₁–c₁), the next one to their gradient representation with the intensity line scans (a₂–c₂), followed by a gradient picture with the adjusted Wulff hulls (a₃–c₃), and the retrieved shapes of the spinel nanocrystals (a₄–c₄). Since the intensity of the HAADF-STEM image depends on the scattering factor and the average atomic number of the projected atomic columns only, it may be used to assess the shape of the cobalt spinel nanocrystals. Random orientation of the nanocrystals minimizes the diffraction contribution to the image contrast, amplifying the direct dependence of the intensity on the crystallite thickness variation. The latter may be enhanced by the image gradient processing. Despite the fact that the observed nanocrystals are not of perfect shapes, owing to the constancy of the interfacial angles (Steno law), the exposed planes can be reliably assigned on the basis of the characteristic angles, as indicated in Figs. 9 and 10a₁–c₁. The lack of gradient changes along the specific plane indicates a constant sample thickness, implying the absence of edges in the scanned region, and hence no change of the faceting (Figs. 8 and 9a₂–c₂). Therefore, taking into account the constraints imposed by the spinel structure ($Fd\bar{3}m$), along with the information about the detected edge patterns and the regions of the constant thickness deduced from gradient image analyses, it was possible to extract the shape of the investigated nanocrystals by using an inverse Wulff construction (Figs. 9 and 10a₄–c₄). In other words, the equilibrium Wulff hull of the cobalt spinel nanocrystal was adjusted to the experimental projected shape, and its orientation was deduced from the detected edge pattern (Figs. 9 and 10a₃–c₃).

In the case of the catalyst obtained by impregnation with an aqueous solution of cobalt nitrate, all of the projected contours have the interplanar angles close to 125° and 145° (Fig. 9a₁–c₁). This suggests an essentially rhombicuboctahedral shape of the investigated nanocrystals. A more detailed analysis revealed that the contrast gradient varies along each of the nanocrystal projections, indicating the variation of the nanocrystals thickness. The lack of the contrast gradient variation in the middle of the nanocrystal projection indicates the presence of the (110) facet (Fig. 9a₂–c₂).

The retrieved rhombicuboctahedral morphologies (Fig. 9a₄–c₄) of the cobalt spinel nanocrystals show the following abundance of the facets: (100) – 47%, (111) – 42% and (110) – 11%. For the glycerol-assisted impregnation (Fig. 10), the projected contour presented in Fig. 10a₁ exhibits the interplanar angles close to 121°, which can be assigned to the interplanar angle between the two neighboring (110) facets, separated by the (111) plane. The lack of the contrast gradient variation in the middle of the

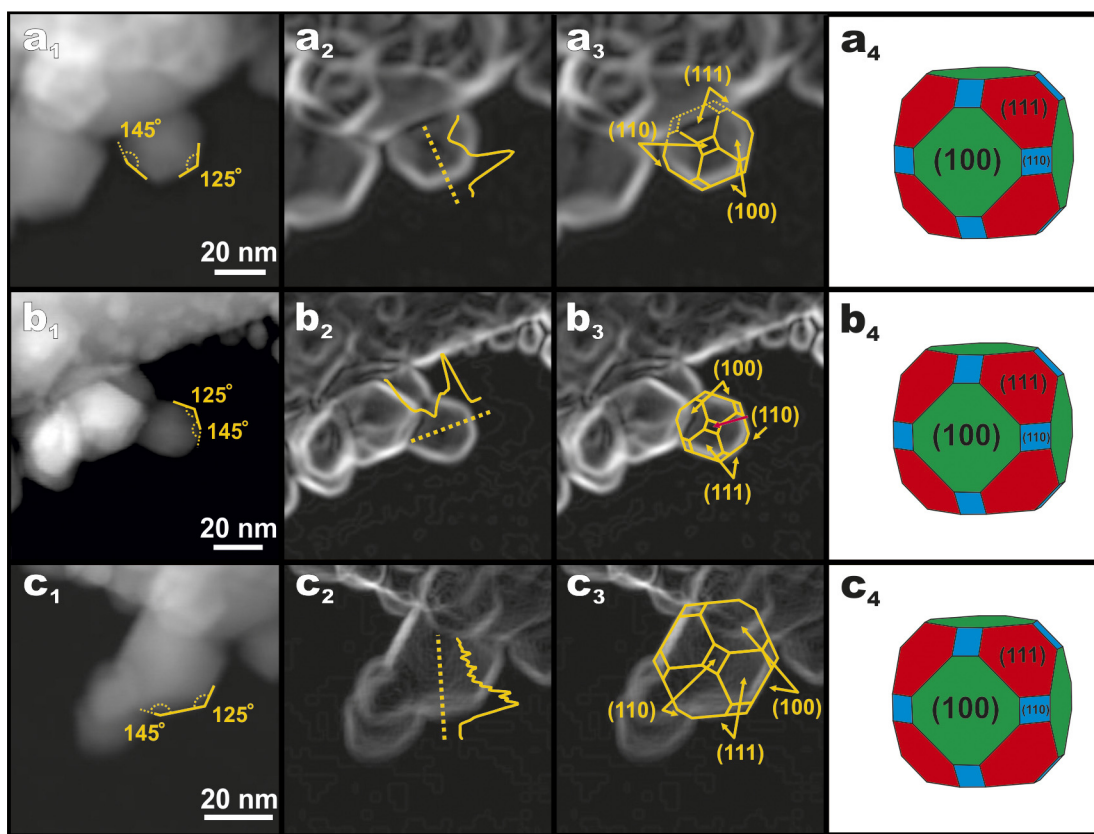


Fig. 9. HAADF/STEM images of morphology of cobalt spinel catalyst obtained by impregnation of alumina with aqueous solution $\text{Co}(\text{NO}_3)_2$ along with the shape retrieval by means of inverse Wulff construction, revealing the preferential exposure of (111) facets.

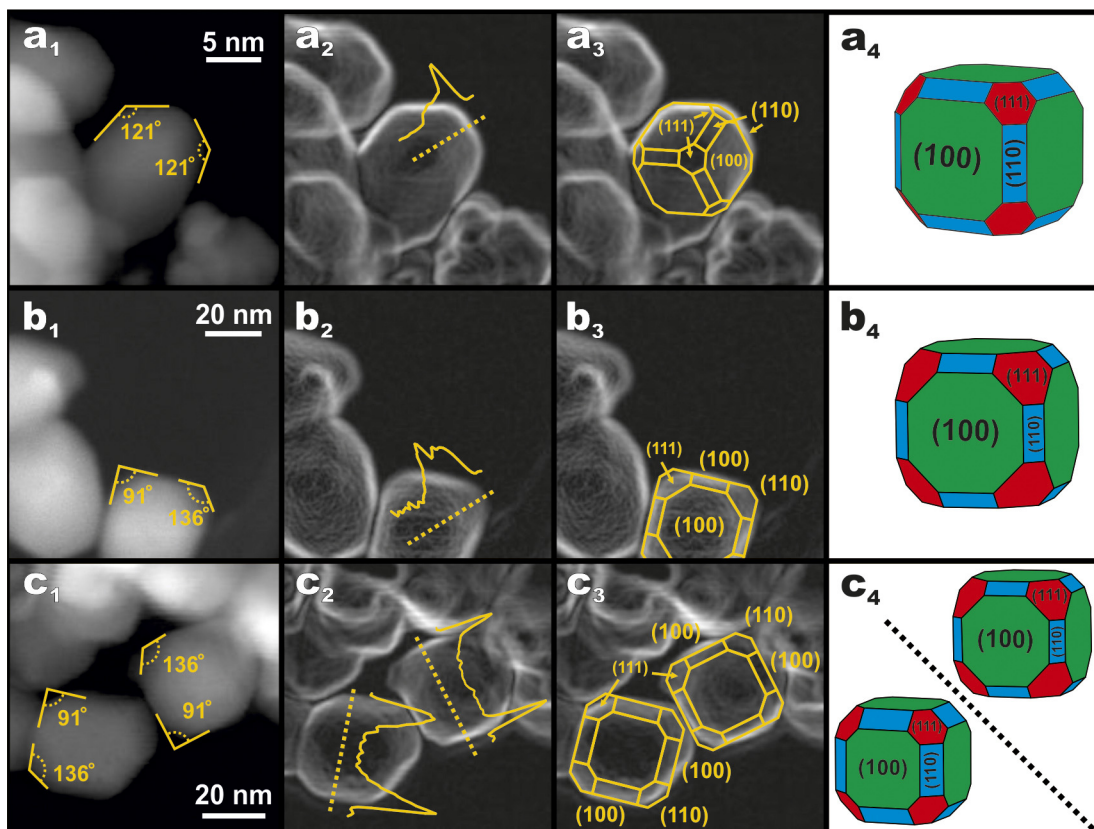


Fig. 10. HAADF/STEM images of morphology of cobalt spinel catalyst obtained by impregnation of alumina with glycerol solution of $\text{Co}(\text{NO}_3)_2$ along with the shape retrieval by means of inverse Wulff construction, revealing the preferential exposure of (100) facets.

nанocrystal projection confirms the presence of the (111) facet (Fig. 10a₂). The retrieved doubly truncated cubic shape (Fig. 10a₄) shows the dominance of the (100) facet (67%) and the lower abundance of the (110) and (111) facets, 20% and 13%, respectively. For other orientations in Fig. 10b–c the interplanar angles are close to 90° and 135°. These values can be assigned to the interplanar angles between the two (100) facets or between the (100) and (110) facets, respectively. Again, the lack of the contrast gradient (Fig. 10b₂–c₂) indicates the constant thickness of the nanocrystals along the view direction, which implies the presence of the (100) facet. The planar shapes of the spinel nanocrystals and the retrieved 3D truncated cubic shapes are presented in Fig. 10a₄–c₄. For the glycerol-assisted samples, the obtained nanocrystallites show the dominance of the (100) facet with the abundance of 65%, 64% (Fig. 10c₄, top) and 58% (Fig. 10c₄, down) for the analyzed nanocrystals. The contribution of the remaining (110) and (111) facets was equal to: 14%, 21% (Fig. 10b₄), 19%, 17% (Fig. 10c₄, top), and 26%, 16% (Fig. 10c₄, down), respectively. Thus, the obtained crystallites exhibit shapes that are far from equilibrium morphology in contrast to the spinel nanocrystals obtained by nitrate decomposition, for which the rhombicubooctahedral morphology is close to the equilibrium one [35]. Despite the small shape variation, the glycerol-assisted method allowed for obtaining the nanocrystals with similar fairly well replicable morphologies.

Summing up the STEM/HAADF investigations and image analysis of the spinel nanocrystals morphology it can be concluded that whereas for the samples prepared from the aqueous solution the (111) plane is approaching the (100) abundance, the glycerol-assisted synthesis leads to the development of the dominant (100) facets. It is also worth mentioning here that whereas on the original STEM images (compare a₁–c₁ and a₂–c₂ in Figs. 9 and 10) the truncations are practically undetectable, yet their presence may be revealed in the gradient representation supported by the Wulff hull matching.

The observed differences in the dispersion and faceting of the spinel nanoparticles may be invoked to explain the observed changes in the catalytic activity and resistance to the presence of contaminants (Fig. 3). The increase in spinel dispersion, by enhancing the number of accessible active sites, leads ubiquitously to higher activity. This is illustrated in Fig. 3c, where the catalytic performance is normalized with respect to the total surface area of the spinel active phase. The surface area normalized reaction rates ($\mu\text{mol}_{\text{N}_2\text{O}} \text{m}^{-2} \text{min}^{-1}$) as a function of temperature show that the dispersion factor, although significant (compare the TPSR profiles in Fig. 3a and c) cannot explain the observed differences completely. This confirms that the catalyst morphology plays an important role herein.

The observed refaceting of the spinel grains, in turn, is additionally responsible for different susceptibility to H_2O , NO_x contaminants. The (100) surface predominant in the $\text{Co}_3\text{O}_4|\alpha\text{-Al}_2\text{O}_3$ catalyst prepared via glycerol-assisted method, due to the lower content of the surface coordinatively unsaturated ions, is much more resistant to poisoning. Indeed the *ab initio* thermodynamic modelling has shown that water desorbs completely from the (100) facets at $T < 250^\circ\text{C}$, whereas in the case of (111) it persists on the surface until $\sim 400^\circ\text{C}$ [35], i.e. the temperature where the onset of the N_2O conversion was observed in dry (Fig. 3a insert) and wet conditions (Fig. 3b).

The beneficial effect of glycerol was discussed in terms of complexation of cobalt and formation of intrapore cobalt glycerolate matrix, which upon calcination is transformed into well dispersed Co_3O_4 nanocrystals. Noting the abundance of glycerol on the market the proposed glycerol-assisted synthesis of the supported $\text{Co}_3\text{O}_4|\alpha\text{-Al}_2\text{O}_3$ catalyst may have considerable practical implications. By the mere addition of 30% of glycerol to impregnation solution the N_2O conversion may be substantially enhanced

in the temperature window of interest for the tertiary abatement of the nitric acid plant. Since the method is cheap, easy to apply and scale-up it can be used for synthesis for other transition metal oxide catalysts.

4. Conclusions

A series of supported $\text{Co}_3\text{O}_4|\alpha\text{-Al}_2\text{O}_3$ catalyst obtained by glycerol-assisted method was synthesized, characterized and their reactivity was evaluated in low temperature N_2O decomposition. The superior activity in comparison to the benchmark $\text{Co}_3\text{O}_4|\alpha\text{-Al}_2\text{O}_3$ catalyst obtained via incipient wetness impregnation with the aqueous solution was accounted for by a better dispersion of the spinel active phase and shape modification of the spinel nanocrystals. Whereas for the samples prepared from the aqueous solution the spinel active phase exhibits a broad bimodal size distribution (with the maxima for 10–50 nm particles and 300–600 nm agglomerates) in the case of glycerol-assisted synthesis the roughly monomodal distribution is featured by the dominant presence of the isolated spinel nanocrystallites of 10–30 nm. At the same time, the presence of glycerol changes the spinel crystallites morphology by decreasing the exposition of the less active (111) planes and increasing the abundance of the more active (100) facets. It was shown that the beneficial effect of glycerol is sustained in the presence of typical residuals (H_2O , NO_x , O_2) in the tail gases of nitric acid plants. The observed effect of glycerol-assisted synthesis was accounted for by complexation of cobalt by glycerol, leading to the formation of intrapore cobalt glycerolate, which upon calcination is transformed into well-dispersed Co_3O_4 nanocrystals dominated by the (100) facets.

Acknowledgment

Authors would like to acknowledge the Polish National Centre for Research and Development funding awarded by the decision number PBS2/A5/38/2013.

Appendix A. Supplementary data

Supplementary data associated with this article can be found, in the online version, at <http://dx.doi.org/10.1016/j.apcatb.2016.08.034>.

References

- [1] J.A. Duro, Ecol. Indic. 66 (2016) 173–179.
- [2] J. Perez-Ramirez, F. Kapteijn, K. Schoffel, J.A. Moulijn, Appl. Catal. B 44 (2003) 117.
- [3] K. Karásková, L. Obalová, F. Kovanda, Catal. Today 176 (2011) 208.
- [4] P. Stelmachowski, G. Maniak, A. Kotarba, Z.J. Sojka, Catal. Commun. 10 (2009) 1062.
- [5] P. Stelmachowski, G. Maniak, J. Kaczmarczyk, F. Zasada, W. Piskorz, A. Kotarba, Z. Sojka, Appl. Catal. B 146 (2014) 105.
- [6] L. Yan, T. Ren, X. Wang, Q. Gao, D. Ji, J. Suo, Catal. Commun. 4 (2003) 505.
- [7] L. Yan, T. Ren, X. Wang, D. Ji, J. Suo, Appl. Catal. B 45 (2003) 85.
- [8] G. Grzybek, P. Stelmachowski, S. Gudyka, J. Duch, K. Cmil, A. Kotarba, Z. Sojka, Appl. Catal. B 168–169 (2015) 509.
- [9] H. Yoshino, C.H. Ohnishi, S. Hosokawa, K. Wada, M. Inoue, J. Mater. Sci. 46 (2011) 797.
- [10] L. Obalová, K. Karásková, A. Wach, P. Kustrowski, K. Mamulová-Kutláková, S. Michalik, K. Jirátová, Appl. Catal. A 462/463 (2013) 227.
- [11] G. Maniak, P. Stelmachowski, F. Zasada, W. Piskorz, A. Kotarba, Z. Sojka, Catal. Today 176 (2011) 369.
- [12] V. Boissel, S. Tahir, C.A. Koh, Appl. Catal. B 64 (2006) 234.
- [13] P.S.S. Reddy, N. Seshu Babu, N. Pasha, N. Lingaiah, P.S. Sai Prasad, Catal. Commun. 9 (2008) 2303.
- [14] S.C. Christoforou, E.A. Efthimiadis, I.A. Vasalos, Catal. Lett. 79 (2002) 137.
- [15] Q. Shen, L. Li, J. Li, H. Tian, Z. Hao, J. Hazard. Mater. 163 (2009) 1332.
- [16] J. Oi, A. Obuchi, G.R. Bamwenda, A. Ogata, H. Yagita, S. Kushiyama, K. Mizuno, Appl. Catal. B 12 (1997) 277.
- [17] A. Bueno-Lopez, I. Such-Basanez, C. Salinas-Martinez de Lecea, J. Catal. 244 (2006) 102.

- [18] J. Yang, L. Lukashuk, J. Akbarzadeh, M. Stöger-Pollach, H. Peterlik, K. Föttinger, G. Rupprechter, U. Schubert, *Chem. Eur. J.* 21 (2015) 885.
- [19] J.-F. Lambert, M. Che, *J. Mol. Catal.* 162 (2000) 5.
- [20] J. Zhao, Y. Liu, M. Fan, L. Yuan, X. Zou, *Inorg. Chem. Front.* 2 (2015) 198.
- [21] D. Mitchell, Dave Mitchell's DigitalMicrograph™ Scripting Website, University of Wollongong, Wollongong, Australia, www.dmscripting.com.
- [22] J. Canny, *Pattern analysis and machine intelligence*, *IEEE Trans.* 6 (1986) 679.
- [23] E. Meijering, FeatureJ, Biomedical Imaging Group of the Swiss Federal Institute of Technology in Lausanne (EPFL), Switzerland, www.imagescience.org/meijering/software/featurej/.
- [24] W.S. Rasband, ImageJ, U.S. National Institutes of Health, Bethesda, Maryland, USA, 2014 (1997) imagej.nih.gov/ij.
- [25] EUROKIN spreadsheet on requirements for measurement of intrinsic kinetics in the gas-solid fixed-bed reactor, (2012), www.eurokin.org.
- [26] V.G. Hadjiev, M.N. Iliev, I.V.J. Vergilov, *J. Phys. C* 21 (1988) L199.
- [27] C. Ehrhard, M. Gjikaj, W. Brockner, *Thermochim. Acta* 432 (2005) 36.
- [28] T. Cseri, S. Bekassy, G. Kenessey, G. Liptyay, F. Figueras, *Thermochim. Acta* 288 (1996) 137.
- [29] F. Zasada, W. Piskorz, Z. Sojka, *J. Phys. Chem. C* 119 (2015) 19180.
- [30] D.M. Reinoso, D.E. Damiani, G.M. Tonetto, *Appl. Catal. B* 144 (2014) 308.
- [31] M. Khalique Ahmed, M.P. McLeod, J. Nézivar, A.W. Giuliani, *Spectroscopy* 24 (2010) 601.
- [32] J. Kaczmarczyk, F. Zasada, J. Janas, P. Indyka, W. Piskorz, A. Kotarba, Z. Sojka, *ACS Catal.* 6 (2016) 1235.
- [33] S. Specchia, C. Galletti, V. Specchia, *Stud. Surf. Sci. Catal.* 175 (2010) 59.
- [34] G. Ercolino, G. Grzybek, P. Stelmachowski, S. Specchia, A. Kotarba, V. Specchia, *Catal. Today* 257 (2015) 66.
- [35] F. Zasada, W. Piskorz, S. Cristol, J.-F. Paul, A. Kotarba, Z. Sojka, *J. Phys. Chem. C* 114 (2010) 22245.